



Simplify your imaging workflows

**Make research imaging workflows accessible, traceable,
and secure with Athena Software for Core Imaging Facilities.**

Thermo Scientific™ Athena Software is a premium imaging data management platform designed for core imaging facilities that support materials science research.

Athena Software ensures traceability of images, metadata, and experimental workflows through an intuitive and collaborative web interface.

Find out more at thermofisher.com/athena

ThermoFisher
SCIENTIFIC

Tunable Fiber-Cavity Enhanced Photon Emission from Defect Centers in hBN

Stefan Häußler, Gregor Bayer, Richard Waltrich, Noah Mendelson, Chi Li, David Hunger, Igor Aharonovich, and Alexander Kubanek*

Realization of quantum photonic devices requires coupling single quantum emitters to the mode of optical resonators. In this work, a hybrid system consisting of defect centers in few-layer hexagonal boron nitride (hBN) grown by chemical vapor deposition and a fiber-based Fabry–Pérot cavity is presented. The sub 10-nm thickness of hBN and its smooth surface enable efficient integration into the cavity mode. This hybrid platform is operated over a broad spectral range larger than 30 nm and its tuneability is used to explore different coupling regimes. Consequently, very large cavity-assisted signal enhancement up to 50-fold and strongly narrowed linewidths are achieved, which is owing to cavity funneling, a record for hBN-cavity systems. Additionally, an excitation and readout scheme is implemented for resonant excitation that allows to establish cavity-assisted photoluminescence excitation (PLE) spectroscopy. This work marks an important milestone for the deployment of 2D materials coupled to fiber-based cavities in practical quantum technologies.

1. Introduction

Atomically thin van der Waals materials have recently attracted increasing attention as nanophotonic platforms due to their unique photophysical properties,^[1] lack of dangling bonds ideal for integration, and unparalleled potential for exploration of light-matter interactions at the nanoscale.^[2–5] For example, the growing family of transition metal di-chalcogenides (TMDCs) is often used to study special exciton effects—e.g., Moire patterns^[6] or exciton–polariton condensates.^[7] On the other hand, hexagonal boron nitride (hBN) has been explored^[8,9] due to its ability to host bright and narrowband optically active luminescent defects that can act as single photon emitters (SPEs)^[10] with very high quantum efficiency approaching 87 %.^[11] Recent progress has further accel-

erated interest in hBN as a quantum photonics platform. Outstanding milestones include demonstration of optically detected magnetic resonance,^[12,13] a strong response to electrical and strain fields,^[14,15] photoluminescence upconversion via anti-Stokes process,^[16] demonstration of Rabi-oscillations and resonance fluorescence^[17] as well as demonstrations of wafer scale growth of single crystal hBN.^[18,19]

One of the outstanding goals in the framework of SPEs in atomically thin materials is their efficient coupling to optical cavities^[20,21] and photonics platforms.^[22,23] Coupled emitter-cavity systems afford increased emission rates and enhanced collection efficiency, both representing critical goals for employing SPEs in scalable nanophotonic devices. Initial experiments with hBN have demonstrated the coupling of defect centers to dielectric photonic crystal cavities and micro-disk resonators,^[24–26] and cavity-enhanced single-photon generation with Fabry–Pérot (FP) cavities in a compact architecture.^[27] However, the successful coupling yield of SPEs to the resonators with these geometries is still low. A critical issue has remained the wide range of emission energies observed for hBN SPEs, with zero-phonon lines (ZPL) known to range from ≈ 550 – 800 nm,^[28,29] making efficient coupling to optical cavities with a fixed resonance wavelength challenging.

In this work, we demonstrate a novel approach to overcome this issue by coupling hBN SPEs to a fiber-based FP open cavity. Our cavities exhibit a high finesse of up to 3000 and small modal volume down to $\approx 68\lambda^3$ or lower for $\lambda = 600$ nm,

S. Häußler, G. Bayer, R. Waltrich, A. Kubanek
Institute for Quantum Optics
Ulm University
Albert-Einstein-Allee 11, D-89081 Ulm, Germany
E-mail: alexander.kubanek@uni-ulm.de

S. Häußler, A. Kubanek
Center for Integrated Quantum Science and Technology (IQst)
Ulm University
Albert-Einstein-Allee 11, D-89081 Ulm, Germany

N. Mendelson, C. Li, I. Aharonovich
School of Mathematical and Physical Sciences
University of Technology Sydney
Ultimo, NSW 2007, Australia

D. Hunger
Physikalisches Institut
Karlsruhe Institute of Technology
Wolfgang-Gaede-Straße 1, D-76131 Karlsruhe, Germany

I. Aharonovich
ARC Centre of Excellence for Transformative Meta-Optical Systems
Faculty of Science
University of Technology Sydney
Ultimo, NSW 2007, Australia

 The ORCID identification number(s) for the author(s) of this article can be found under <https://doi.org/10.1002/adom.202002218>.

© 2021 The Authors. Advanced Optical Materials published by Wiley-VCH GmbH. This is an open access article under the terms of the Creative Commons Attribution License, which permits use, distribution and reproduction in any medium, provided the original work is properly cited.

DOI: 10.1002/adom.202002218

which is ideal for coupling to hBN SPEs. Most importantly, these cavities offer a unique advantage for the integration of 2D materials. The full tunability of the cavity among all three lateral dimensions over several μm enables not only the simultaneous investigation of many SPEs within a single hBN membrane (lateral tunability), but also the study of SPEs with varying emission energies (vertical tunability). We utilize a thin membrane of hBN via chemical vapor deposition (CVD), which are advantageous over other hBN material sources as they provide a high surface quality to minimize scattering losses, and enable control over the photophysical properties of the defects during growth.^[30,31]

2. Experimental Platform

Spectroscopic measurements were performed using a custom-built confocal microscope with an NA = 0.7 microscope objective combined with a micro resonator setup consisting of a macroscopic planar mirror and a fiber mirror. Both, the planar and the fiber mirror are provided with a highly reflective dielectric coating to form a distributed Bragg reflector (DBR). The DBR stack of the planar mirror is designed for high reflectivities in the spectral range common for hBN SPEs (i.e., from 560 to 740 nm) with a transmission of 500 ppm at 615 nm and has a high index termination, which leads to a field node on the surface of the mirror. The fiber mirror is fabricated with a concave structure having a radius of curvature (ROC) of $R_c = 35 \mu\text{m}$, which was produced by laser ablation from a high

power CO₂ laser before coating. The ROC of the structure is estimated from a parabolic fit to an interferometer image enabling resonator lengths L_0 of more than 30 μm in stable operation. The homogeneous ablation of material from the high intensity infrared laser leads to a relatively smooth surface enabling high finesse values.^[32] The reflectivity of the fiber mirror ranges from 560 to 660 nm. This asymmetry was chosen such that collection of fluorescence with shorter wavelengths is favored through the planar mirror. Both dielectric coatings are transmissive for green (532 nm) laser light, enabling off-resonant excitation of color centers inside the resonator. The length of the fiber cavity (z -direction) is tunable via the fiber mirror side while the planar mirror can be adjusted in the lateral direction (x - and y -direction). A schematic representation of the platform is shown in Figure 1a.

Switching between scannable confocal microscope and fiber-cavity based collection mode is possible by flipping the planar mirror. First, we characterize the bare fiber-cavity (without hBN) via the fiber mirror side. We measure the spectrum of the fiber resonator by recording the transmission of a broadband light source with a grating spectrometer for different cavity lengths. For an exemplary length of $L_0 = 10.66 \mu\text{m}$, the transmission spectrum is depicted in Figure 1b resulting in a cavity free spectral range (FSR) of $\Delta\lambda_{\text{FSR}} = 16.89 \text{ nm}$ at 600 nm ($\Delta\nu_{\text{FSR}} = 14.07 \text{ THz}$). The spectral position of the fundamental modes for a given cavity length are utilized to calculate and compensate the piezo hysteresis by applying a third order polynomial function to the measured data (details see Supporting Information).

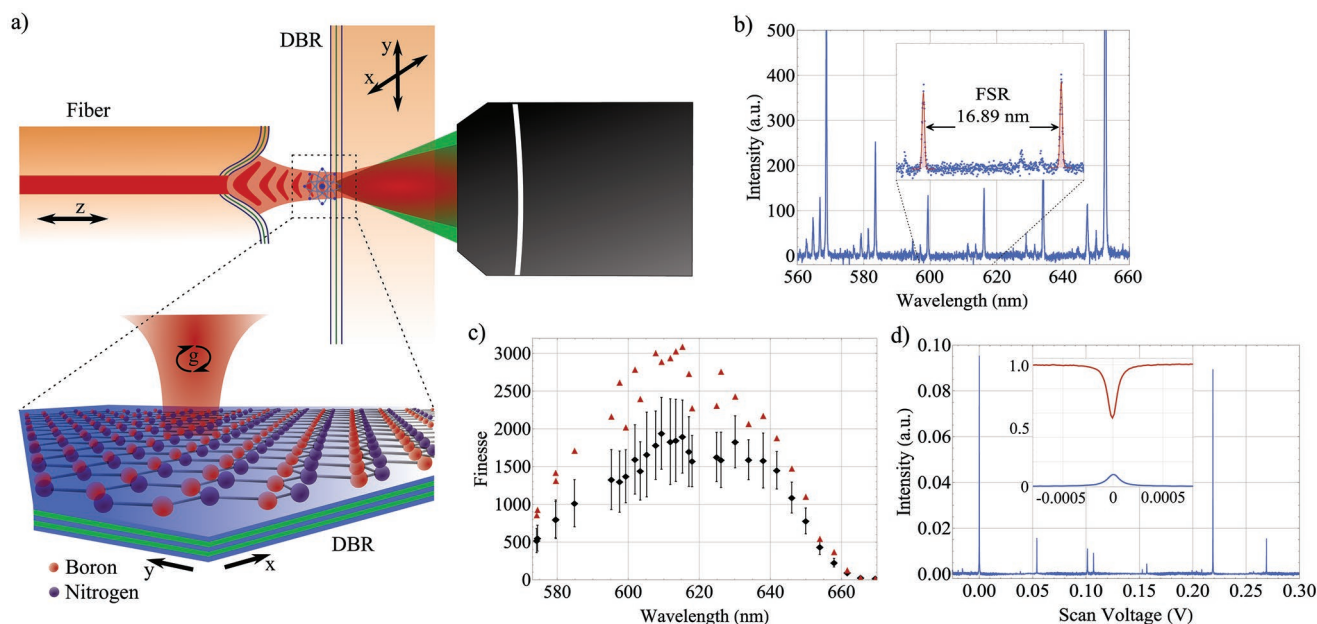


Figure 1. a) Design of the micro resonator setup. A macroscopic planar mirror and the tip of a glass fiber with concave structure form a plano-concave resonator. A CVD grown hBN membrane is placed on the planar mirror forming a hybrid quantum emitter fiber-cavity system. b) Cavity transmission spectrum in the wavelength range from 560 to 660 nm revealing a cavity free spectral range (FSR) of $\Delta\lambda_{\text{FSR}} = 16.89 \text{ nm}$ at 600 nm. c) Cavity finesse \mathcal{F} as a function of the wavelength determined by scanning cavity measurements. The data (black diamonds) is averaged over several scans, while maximum values of single scans (red triangles) >3000 are reached between 600 and 620 nm. The finesse decays to the higher (lower) wavelength side due to the limited mirror reflectivities. d) Cavity transmission versus piezo voltage over one cavity FSR. We observe strong coupling to the fundamental mode, while higher order modes are weakly pronounced. The inset shows the transmitted (blue) and reflected (red) signal at resonance. The maximum coupling efficiency visible in the reflection measurement is limited by the impedance mismatch of the fiber mirror and the cavity mode.

We determine the cavity finesse \mathcal{F} by measuring the transmission of a narrowband (100 kHz) dye ring laser system while continuously scanning the cavity length. The cavity finesse is defined as the ratio of the FSR and the FWHM linewidth of the resonances $\mathcal{F} = \text{FSR} / \text{FWHM}$. High finesse values of up to 3000 are obtained in the wavelength range between 600 and 620 nm, while the finesse decreases for higher (lower) wavelengths due to decreasing mirror reflectivity of the fiber (planar) mirror (Figure 1c). Variations in the finesse result from mechanical noise during the scans. The cavity length can be varied within the theoretically predicted stability regime without significant changes of the finesse (see Supporting Information). However, in this work we focus on short cavity lengths (<15 μm) for increased coupling between SPE and cavity mode (for detailed calculations see Supporting Information). The transmission through the scanning cavity (Figure 1d) displays pronounced fundamental modes, while coupling to higher order modes appears strongly suppressed. This indicates precise alignment of the resonator, yielding the best possible quality of the resonator modes. The maximum coupling efficiency of the laser light into the cavity mode is extrapolated from the reflection measurement (red curve in the inset of Figure 1d) and yields 45 %. The efficiency is limited by the impedance mismatch between the fiber end and the cavity mode.

3. Sample Characterization

The sample is fabricated using large scale thin layers of hBN grown by CVD on copper, as described in detail in reference.^[33] The hBN membrane is sandwiched between two PMMA layers of 95 nm thickness to position the defects in the field maximum of the cavity mode, and transferred to the planar mirror. The hBN membrane is then first examined via confocal microscopy at room temperature using an off-resonant laser (DPSS) at 532 nm. An exemplary confocal scan of a $50 \times 50 \mu\text{m}^2$ region is shown in Figure 2a. We record photoluminescence (PL) spectra of numerous defects revealing that the hBN hosts a large variety of defects covering a broad wavelength range from ≈ 570 nm up to 740 nm. The majority of defects emit between 570 and 590 nm, as reported in the references.^[30,31,33,34] A PL spectrum of such a defect (marked spot in Figure 2a) features pronounced zero-phonon line (ZPL) emission centered at $\lambda \approx 632$ nm with a FWHM linewidth of $\delta\lambda = 3.3$ nm and a phonon sideband (PSB) up to ≈ 740 nm. The linewidth of the investigated defects spreads from 3 nm to more than 20 nm (Figure 2b). Emitter stability was not systematically investigated, but proved to be high for a few emitters.

The scattering losses due to the inserted hBN membrane inside the resonator are investigated by recording a transmission intensity map of the broadband light source (see Figure 2c). Here, the intensity of cavity modes in the spectral range between 570 and 650 nm is summed up and plotted. Additionally, we measure the finesse of the cavity on several regions on the hBN membrane (marked spots in Figure 2c) and extract the scattering losses introduced by the membrane (cf. Table 1), as it has been done for a diamond membrane cavity system.^[35] For reference, a finesse of 480, as it can be found on average over large areas, corresponds to an rms surface

roughness of $\sigma = 4.1$ nm of the hBN membrane. Furthermore, atomic force microscopy (AFM) is applied - measured on SiO_2 after removing the PMMA used for the transfer with hot acetone and prior to hBN encapsulation between the two PMMA layers—to determine the overall height of the hBN membrane. An AFM scan of the hBN membrane edge ($10 \times 10 \mu\text{m}^2$) with a resolution of $512 \times 512 \text{ px}$ is shown in Figure 2d. The height trace along the white dashed line yields an average membrane thickness of $t_{\text{hBN}} \approx 9.1$ nm and a surface roughness of few nm. From the optical investigations, we conclude that the surface quality in most parts of the PMMA encapsulated hBN membrane is sufficiently high to maintain high finesse and that it therefore is suitable for integration into the cavity mode. We note that variations in surface roughness, primarily a result of wrinkling during the transfer process, lead to variations in the effective cavity finesse, with smoother areas providing higher finesse values. However, additional optimization of the growth process, or additional polishing of the hBN membrane after growth can further improve the obtained results.

4. Coupled System

The planar mirror is now moved laterally to overlap the position of individual defect centers in the hBN membrane with the cavity mode. We utilize the unique scattering map recorded in cavity transmission to make sure that the very same emitter is coupled to the cavity mode that was characterized in confocal spectroscopy before. Off-resonant excitation (at 532 nm) as well as the collection of the cavity mode is done via the planar mirror side. We observe coupling of the defect presented in Figure 2a with a ZPL centered at $\lambda = 632$ nm to a single mode (TEM_{00}) of the fiber-cavity. The cavity-coupled hBN spectrum is presented in Figure 3a (low resolution (0.52 nm/px)), while the inset displays the corresponding high resolution (0.06 nm/px) spectrum at a cavity length of $L_0 = 15.12 \mu\text{m}$. The background signal visible in Figure 3a originates from fiber fluorescence (650 to 750 nm) and surrounding defects (570 to 600 nm). Cavity filtering can be observed by the more than (18 ± 2) -fold reduction of the ZPL linewidth of the defect now dictated by the corresponding cavity linewidth (see inset in Figure 3a). An error discussion can be found in the SM. Note that the cavity length is not actively stabilized, meaning that all broadening effects like the cavity jitter are accumulated during the acquisition of the spectrum. Active stabilization of the cavity length can further reduce the emitter linewidth significantly down to a minimum value on the order of 0.03 nm for this cavity length and $\mathcal{F} = 550$ which was measured for $\lambda = 632$ nm on this spot. Next, we tune the cavity resonance (by scanning the cavity length) over the ZPL frequency of the defect and observe a resonance at $\lambda \approx 632$ nm (Figure 3b). Since we operate in the weak coupling regime, the free-space linewidth of the emitter is recovered when integrating over all spectra for the scan in Figure 3b. A Lorentzian fit yields again approximately the ZPL linewidth of the defect in free-space emission (Figure 3c).

Furthermore, we observe linear polarized emission of the coupled defect with high polarization contrast aligned with the polarization axis of the cavity (see Figure 3d) leading to increased coupling between defect and cavity mode. The high

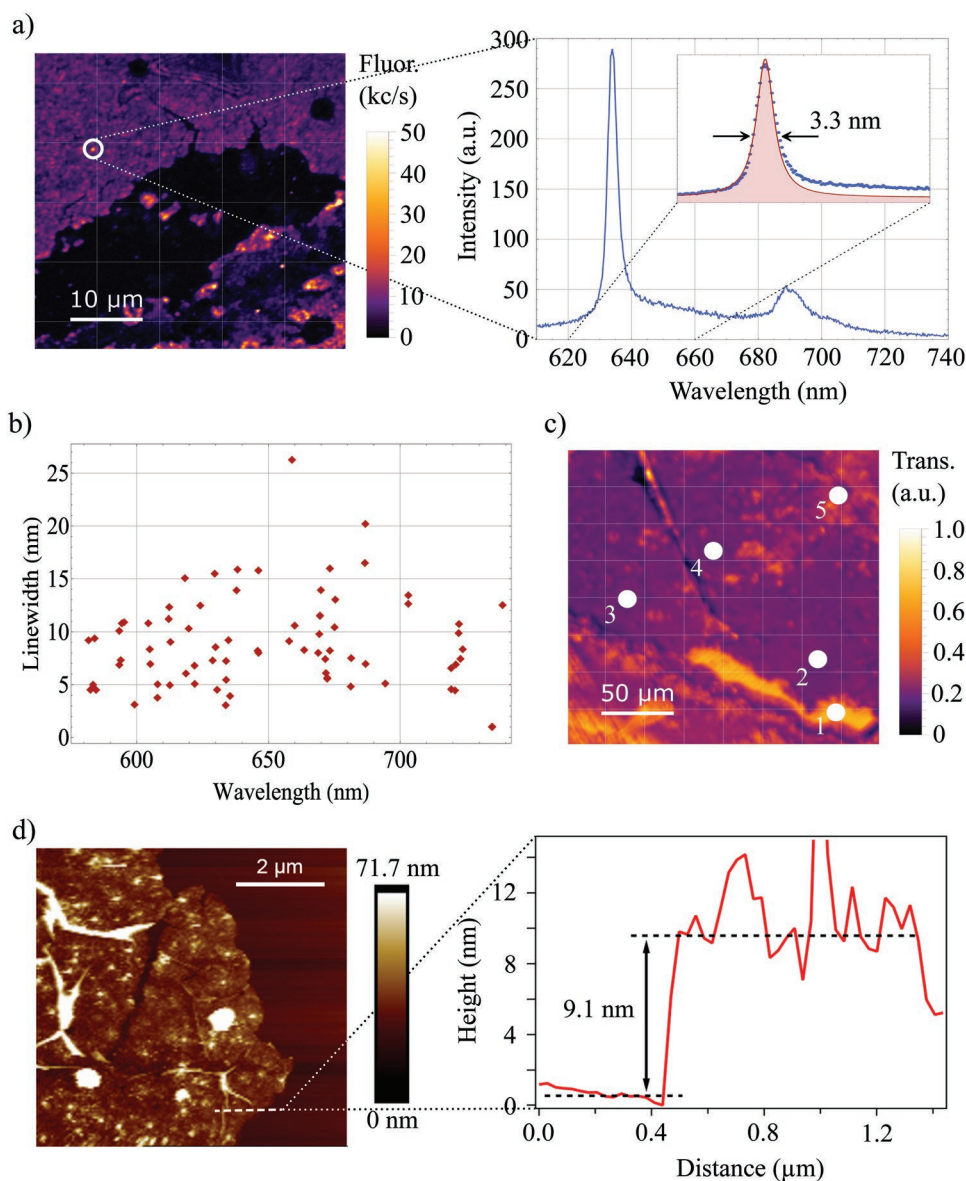


Figure 2. a) Confocal image of a $50 \times 50 \mu\text{m}^2$ region of the CVD grown hBN membrane on the DBR. The PL spectrum of the marked defect exhibits strong ZPL emission at $\lambda \approx 632 \text{ nm}$ with a FWHM linewidth of $\delta\lambda = 3.3 \text{ nm}$ and PSB up to $\approx 740 \text{ nm}$. ZPL center position and linewidth are extracted from a Lorentzian fit (red line in the inset) and deviation of the data for longer wavelengths originates from the presence of the PSB. b) Scatter plot of a fraction of observed emitter wavelengths and linewidths in the CVD grown hBN membrane ranging from 570 to 740 nm to show the variety of present emitters. The FWHM linewidths spread from 3 to 27 nm. c) Cavity transmission intensity map of a broadband light source to investigate the performance of the hBN membrane in the cavity. The cavity finesse is measured on the marked spots to estimate the scattering behavior of the membrane. d) Atomic force microscopy scan of a $10 \times 10 \mu\text{m}^2$ region of the CVD grown hBN membrane. The height trace taken from the white dashed line yields a membrane thickness of $t_{\text{hBN}} \approx 9.1 \text{ nm}$.

polarization contrast mainly originates from the defect itself, since in the regime with $\mathcal{F} < 3000$, the cavity polarization modes are quasi degenerate, lowering the polarization contrast of the cavity. Both polarization patterns were extracted by taking a spectrum for various polarizer angles and determining the maximum intensity of the mode of interest. The cavity mode was mapped out with white light transmission while the coupled emitter was excited with the green laser. A second-order autocorrelation measurement with the polarizer set parallel to the emitter polarization to suppress randomly polarized light

and a 635/10 nm band-pass filter in the detection at an excitation power far from saturation clearly proves single photon emission from the coupled system (see Figure 3e). The anti-bunching dip reaches a minimum value of $g^{(2)}(0) = 0.4$, limited by background fluorescence from surrounding defects. Furthermore, a time constant of $\tau_0 = 2.65 \text{ ns}$ is extracted from an exponential fit, corresponding to a 2-level system model, to the data. The single photon purity of the emission into the cavity mode is further indicated by the high polarization contrast achieved, supporting evidence of a single dipole, as well as the

Table 1. Scattering losses introduced by the hBN membrane.

Spot number	Finesse	Scattering losses
1 (mirror)	2248	1400 ppm
2	465	5360 ppm
3	375	6980 ppm
4	195	14710 ppm
5	886	2150 ppm

reproduction of the freespace ZPL linewidth and position when tuning the cavity resonance across the emitter ZPL.

To further establish cavity-assisted enhancement and cavity funneling, we investigate the coupling of numerous defects at different wavelengths to the cavity mode. In each case, the TEM₀₀-mode of the cavity is tuned into resonance with the ZPL of the particular defect. Note that in free-space an emitter with its dipole in plane with the planar mirror is most efficiently detected. The same dipole alignment is optimal for coupling to the TEM₀₀-mode. As a result, we observe strong cavity funneling of the ZPL emission of these defects into the cavity mode. To classify the effect of the cavity, we extract the spectral enhancement of each ZPL in the cavity mode as well as the reduction of its linewidth by comparing the free space emission with the cavity coupled emission. In total, spectral enhancement is studied for more than 20 defects in the wavelength range between 560 and 600 nm for two different cavity lengths $L_0 = 7 \mu\text{m}$ and $L_0 = 13 \mu\text{m}$ (see Figure 4a). As expected, the largest enhancement values are obtained for very short cavity lengths, while the correspondingly broader cavity resonances lead to less narrowing. At $L_0 = 7 \mu\text{m}$, most defects are more

than 20-fold enhanced, while selected defects exhibit enhancement values of up to 50. At $L_0 = 13 \mu\text{m}$, however, the largest enhancement (6.3) is observed for a defect centered at $\approx 572 \text{ nm}$.

The large spectral enhancement in a well-defined optical mode of the cavity is based on two effects. First, the Purcell factor explains the increased emitter-cavity coupling growing with shorter cavity length. We experimentally confirm this by measuring the spectral enhancement for the two cavity lengths $L_0 = 7 \mu\text{m}$ and $L_0 = 13 \mu\text{m}$. We estimate the effective Purcell factor in the bad emitter regime (cf. ref. [36]) for a strongly dissipative quantum emitter coupled to a high quality cavity for different cavity lengths resulting in a Purcell factor of $F_p \approx 1$ for $L_0 = 7 \mu\text{m}$, 2.3 times higher than for $L_0 = 13 \mu\text{m}$ (details see Supporting Information). Second, the slightly asymmetric coating of the two cavity mirrors ($T_{\text{planar}} > T_{\text{fiber}}$) for wavelengths $< 600 \text{ nm}$ and the overall higher transmission at lower wavelength are designed for high out-coupling rates ($T_{\text{planar}} / (T_{\text{planar}} + T_{\text{fiber}} + L)$) on the planar mirror side (see also Figure 1b,c). The apparent wavelength dependency of the collection enhancement and linewidth narrowing can be explained with the coating. Longer wavelengths have a higher \mathcal{F} , therefore leading to stronger narrowing but also to more signal loss due to increasing scattering. Furthermore, an increasing fraction of the fluorescence is emitted through the fiber mirror side reducing the detected signal through the planar mirror.

In both cases (free space and cavity coupled), we use identical excitation conditions, in particular, the same intensity and numerical aperture optics. The power was chosen to be far below saturation. Since the mirror coatings are transparent at 532 nm, we do not observe any modulation of the transmitted power of the green excitation laser with respect to the cavity length. Therefore, we neglect interference effects of intra cavity

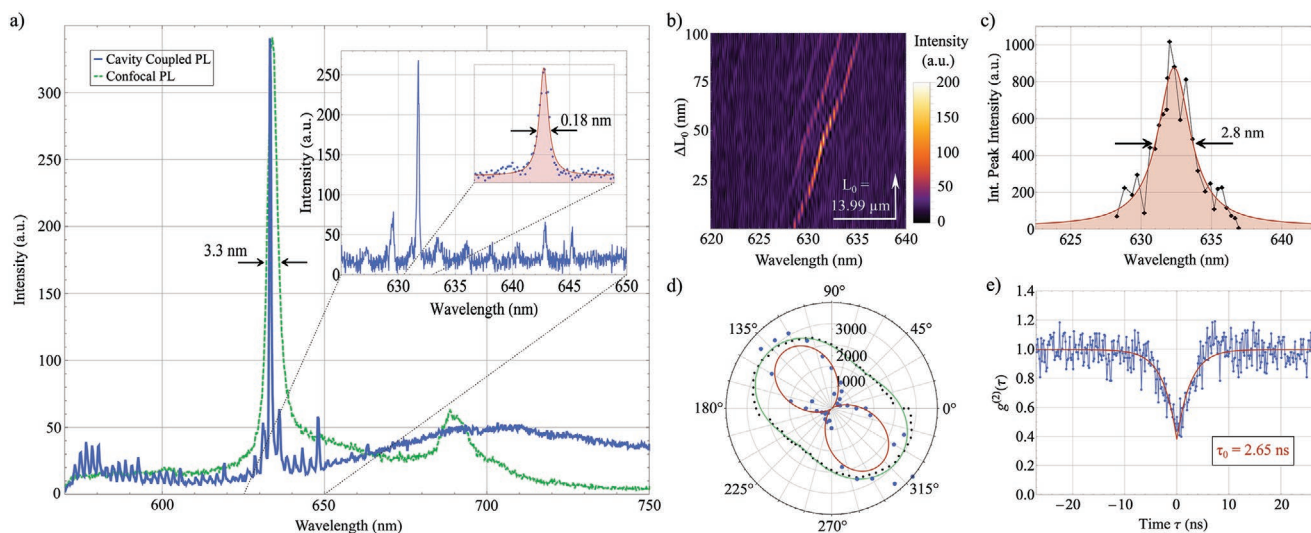


Figure 3. Optical properties of the coupled defect at $\lambda = 632 \text{ nm}$ (PL spectrum in Figure 2a), measured below saturation. a) Cavity coupled (blue) at a cavity length of $L_0 = 15.12 \mu\text{m}$ and free space (green) spectrum represents pronounced cavity filtering of the emission into a single optical mode of the cavity with a more than (18 ± 2) -fold reduced ZPL linewidth. The inset shows the high-resolution image from where the linewidth of $\delta\lambda = 0.18 \text{ nm}$ is extracted from a Lorentzian fit. b) High-resolution cavity coupled fluorescence spectra for different resonance wavelengths $L_0 + \Delta L_0$ starting at $L_0 = 13.99 \mu\text{m}$. c) Integrated cavity fluorescence intensity of the defect for different resonance wavelengths of the cavity. Peak intensity is observed at the center of the defect ZPL. d) Emission polarization of the coupled defect (blue data, red fit) shows preferential emission into the polarization axis of the cavity (black data, green fit) with high polarization contrast. e) Raw second-order autocorrelation measurement histogram of the coupled defect clearly indicates single photon emission with the parameters $g^{(2)}(0) = 0.4$ and $\tau_0 = 2.65 \text{ ns}$.

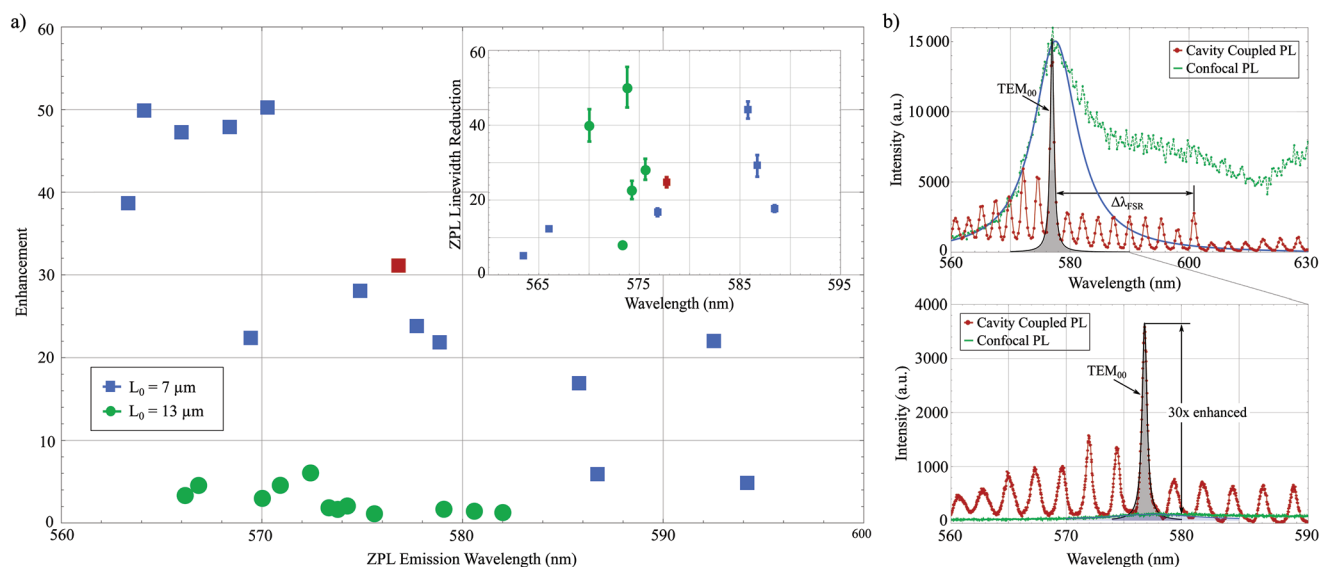


Figure 4. a) Spectral enhancement for different fluorescing defects in the wavelength range from 560 to 600 nm for two different cavity lengths $L_0 = 7 \mu\text{m}$ (blue data) and $L_0 = 13 \mu\text{m}$ (green data). The data point of the defect in (b) is marked red. The inset shows the corresponding reduction of the ZPL linewidth for selected defects. The different factors of linewidth narrowing can be explained by different finesse values as well as different freespace linewidths of the observed spots. b) Cavity coupled spectrum (red) and free space PL spectrum (green) of a defect with its ZPL centered at $\lambda \approx 577 \text{ nm}$ (top). A Lorentzian line shape (blue curve) was used to fit the emitter ZPL. The fluorescence of the ZPL in the cavity is spectrally enhanced by a factor of 30 compared to the free space emission which we extracted from the high-resolution image (bottom), which has less counts per bin due to the finer resolution.

intensity modulations when exciting with 532 nm laser light. The resulting signal enhancement arises from cavity funneling and efficient fluorescence collection when coupled to the cavity mode. To illustrate the determination of the enhancement factor, the cavity coupled spectrum of a defect at $\lambda \approx 577 \text{ nm}$ (red data in Figure 4a) is shown in Figure 4b. Multiple cavity modes are fed by the broadband fluorescence of the defect center. The strongest mode overlaps with the central wavelength of the ZPL at $\lambda = 577 \text{ nm}$, demonstrating a peak spectral enhancement factor of 30 compared to the free space emission (green data in Figure 4b).

Recently, mechanically isolated defect centers have been demonstrated under resonant excitation yielding narrow linewidths up to 60 MHz at room temperature.^[37,38] To access this regime, we establish a method to perform cavity-assisted photoluminescence excitation (PLE) spectroscopy comparable to the scheme presented in reference^[39]. We resonantly excite a defect with its ZPL centered at $\lambda \approx 575 \text{ nm}$ (the ZPL was characterized under off-resonant excitation as depicted in Figure 5a) and detect the PSB in the lower order fundamental q modes of the cavity as shown in Figure 5b. Analogously to Figure 3c, the data in Figure 5a evidences that a negligible amount of background is funneled into the resonator when the cavity is tuned over the ZPL of the emitter at $\approx 572 \text{ nm}$. As an excitation light source, we use here a tunable optical-parametric oscillator (OPO) with second-harmonic-generation (SHG) unit that is tuned on resonance with cavity and emitter ZPL. Therefore, both excitation and collection channel are enhanced by resonant cavity modes. To our knowledge, this is the first evidence of cavity-assisted PLE for defects in hBN. To prove the resonant excitation, we detune the excitation laser from the cavity resonance observing no signal. In addition, we do not observe emission

when the cavity is on resonance with the excitation laser but laterally displaced from the position of the defect (by shifting the planar mirror). We further measure the PLE intensity of a defect center under resonant and near-resonant excitation by tuning the excitation wavelength over the ZPL (Figure 5c). Hereby we continuously keep the cavity on resonance with the excitation laser and normalize the intensity to the transmitted laser power. The displayed integrated intensity corresponds to the cumulative intensity of the fundamental modes in the PSB (cf. Figure 5b). We determine the accumulated lineshape including all broadening effects like dephasing and spectral diffusion in PLE spectroscopy and find it in agreement with the PL lineshape. However, on the short-wavelength side of the ZPL, the near-resonant excitation via acoustic phonon modes becomes apparent. In the presented case, the electron-phonon density of states for the acoustic phonon branch is gap-less and merges into the ZPL. This leads to a reduced excitation efficiency under resonant excitation at room temperature. At the same time, the emission enhancement induced by the cavity is limited by the strong dephasing of the investigated defect center. We extrapolate the achieved cavity enhancement for a defect exhibiting Fourier-Transform limited lines at room temperature as it is reported in the references^[37,38] resulting in Purcell factors >100 assuming ideal emitter-cavity coupling (details see Supporting Information).

5. Conclusion

In summary, we have studied the coupling of quantum emitters in few-layer CVD grown hBN to open, directly fiber-coupled FP cavities. We have demonstrated record cavity-enhanced

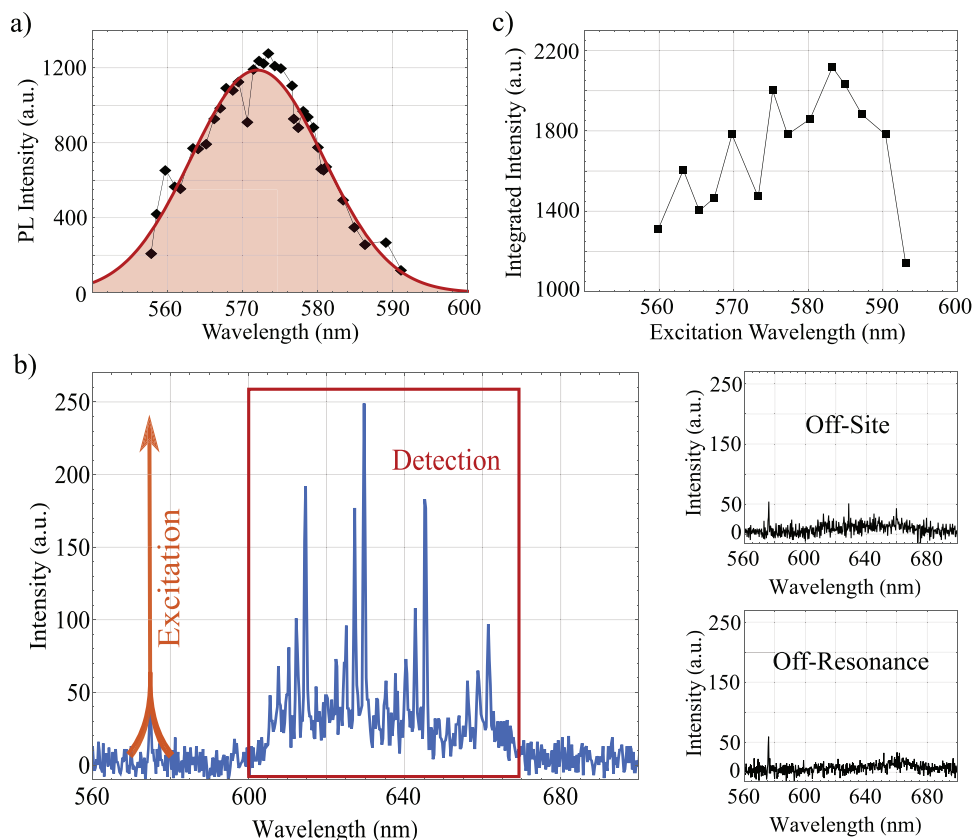


Figure 5. a) Integrated cavity coupled PL intensity of the ZPL under off-resonant excitation for different resonance wavelengths of the cavity, indicating that no significant amount of background is being funneled into the resonator mode. b) Resonant excitation scheme, which shows the excitation at approximately the center of the ZPL at $\lambda = 575$ nm and the detection of the side band in the range 600–680 nm. We do not observe any signal from the defect with the excitation laser on-resonance with the cavity but the cavity mode laterally detuned from the defect (top right) nor with the cavity mode on-site but the laser off-resonance (bottom right). c) Excitation efficiency of the defect over the excitation wavelength. We observe a strong decay starting at ≈ 590 nm. On the lower wavelength side, the decay is not as steep due to the higher probability for off-resonant excitation.

emission for defect centers in hBN. Few defects show up to 50-fold spectral enhancement of their ZPL emission and strong linewidth reduction both owing to cavity funneling. Importantly, our hybrid system offers a broad spectral tuning range ideal for coupling to the wide range of ZPL emission energies common to hBN, demonstrated here by coupling defect centers with emission wavelengths ranging from 565 to 635 nm while being able to demonstrate single-photon emission. Our work paves the way for indistinguishable single photon emission at high rates with potential for enhancing spin readout and for fiber-based quantum photonics with applications in quantum communication.

We further establish cavity-assisted PLE spectroscopy which can be utilized in the future to characterize mechanically isolated defect centers in hBN at room temperature^[37] with critically enhanced photon flux. Making use of cavity-assisted excitation is essential to reduce the necessary excitation power. Since spectral diffusion is power-dependent, our platform can be utilized to overcome spectral instability, which is a prevalent issue in the deployment of hBN SPEs for practical applications. Dissipation in our coupled system is currently limited by rapid emitter dephasing. Extending our work to mechanically

isolated defect centers could eliminate emitter dephasing reaching the Fourier-Transform limit and resulting in emitter linewidth of $\gamma_0 \approx 60$ MHz at room temperature. Our results therefore hold the unique capability to establish a strongly coupled solid-state system with a cooperativity exceeding $C_0 > 100$ at room temperature.

Supporting Information

Supporting Information is available from the Wiley Online Library or from the author.

Acknowledgements

Experiments performed for this work were operated using the Qudi software suite.^[40] S.H. and A.K. acknowledge support of IQst. A.K. acknowledges support from the Baden-Württemberg Stiftung in project Internationale Spitzenforschung. I.A. acknowledges the generous support provided by the Alexander von Humboldt Foundation and the Australian Research council (DP180100077). D.H. acknowledges support by the Karlsruhe School of Optics & Photonics (KSOP).

Open access funding enabled and organized by Projekt DEAL.

Conflict of Interest

The authors declare no conflict of interest.

Author Contributions

S.H. and G.B. contributed equally to this work. S.H., G.B., R.W., and A.K. conceived the experiments, performed the measurements, and evaluated the data. D.H. fabricated the fiber mirrors. N.M., C.L., and I.A. prepared the hBN samples and performed the transfer onto the mirrors. The manuscript was written by S.H. and A.K., and all authors discussed the results and contributed to the manuscript.

Data Availability Statement

Research data are not shared.

Keywords

fiber cavity, hexagonal boron nitride, quantum photonics, single photon emitters

Received: December 21, 2020

Revised: April 9, 2021

Published online:

-
- [1] X. Liu, M. C. Hersam, *Nat. Rev. Mater.* **2019**, *4*, 669.
- [2] P. Rivera, H. Yu, K. L. Seyler, N. P. Wilson, W. Yao, X. Xu, *Nat. Nanotechnol.* **2018**, *13*, 1004.
- [3] Y. Shimazaki, I. Schwartz, K. Watanabe, T. Taniguchi, M. Kroner, A. Imamoğlu, *Nature* **2020**, *580*, 472.
- [4] C. Chakraborty, N. Vamivakas, D. Englund, *Nanophotonics* **2019**, *8*, 2017.
- [5] J. D. Caldwell, I. Aharonovich, G. Cassaboais, J. H. Edgar, B. Gil, D. N. Basov, *Nat. Rev. Mater.* **2019**, *4*, 552.
- [6] B. Blasius, L. Rudolf, G. Weithoff, U. Gaedke, G. F. Fussmann, *Nature* **2020**, *577*, 226.
- [7] S. Dufferwiel, S. Schwarz, F. Withers, A. A. P. Trichet, F. Li, M. Sich, O. Del Pozo-Zamudio, C. Clark, A. Nalotov, D. D. Solnyshkov, G. Malpuech, K. S. Novoselov, J. M. Smith, M. S. Skolnick, D. N. Krizhanovskii, A. I. Tartakovskii, *Nat. Commun.* **2015**, *6*, 8579.
- [8] K. Watanabe, T. Taniguchi, T. Niiyama, K. Miya, M. Taniguchi, *Nat. Photonics* **2009**, *3*, 591.
- [9] G. Cassaboais, P. Valvin, B. Gil, *Nat. Photonics* **2016**, *10*, 262.
- [10] A. Bommer, C. Becher, *Nanophotonics* **2019**, *8*, 2041.
- [11] N. Nikolay, N. Mendelson, E. Özelci, B. Sontheimer, F. Böhm, G. Kewes, M. Toth, I. Aharonovich, O. Benson, *Optica* **2019**, *6*, 1084.
- [12] A. Gottscholl, M. Kianinia, V. Soltamov, S. Orlinskii, G. Mamin, C. Bradac, C. Kasper, K. Krambrock, A. Sperlrich, M. Toth, I. Aharonovich, V. Dyakonov, *Nat. Mater.* **2020**, *19*, 540.
- [13] N. Chejanovsky, A. Mukherjee, Y. Kim, A. Denisenko, A. Finkler, T. Taniguchi, K. Watanabe, D. Bhaktavatsala Rao Dasari, J. H. Smet, J. Wrachtrup, *arXiv:1906.05903*, **2019**.
- [14] N. Nikolay, N. Mendelson, N. Sadzak, F. Böhm, T. T. Tran, B. Sontheimer, I. Aharonovich, O. Benson, *Phys. Rev. Appl.* **2019**, *11*, 041001.
- [15] Y. Xia, Q. Li, J. Kim, W. Bao, C. Gong, S. Yang, Y. Wang, X. Zhang, *Nano Lett.* **2019**, *19*, 7100.
- [16] Q. Wang, Q. Zhang, X. Zhao, X. Luo, C. Pei Yu Wong, J. Wang, D. Wan, T. Venkatesan, S. J. Pennycook, K. Ping Loh, G. Eda, A. T. S. Wee, *Nano Lett.* **2018**, *18*, 6898.
- [17] K. Konthasinghe, C. Chakraborty, N. Mathur, L. Qiu, A. Mukherjee, G. D. Fuchs, N. Vamivakas, *Optica* **2019**, *6*, 542.
- [18] T.-A. Chen, C.-P. Chuu, C.-C. Tseng, C.-K. Wen, P. H. S. Wong, S. Pan, R. Li, T.-A. Chao, W.-C. Chueh, Y. Zhang, Q. Fu, B. I. Yakobson, W.-H. Chang, L.-J. Li, *Nature* **2020**, *579*, 219.
- [19] J. S. Lee, S. H. Choi, S. J. Yun, Y. I. Kim, S. Boandoh, J.-H. Park, B. G. Shin, H. Ko, S. H. Lee, Y.-M. Kim, Y. H. Lee, K. K. Kim, S. M. Kim, *Science* **2018**, *362*, 817.
- [20] L. C. Flatten, L. Weng, A. Branny, S. Johnson, P. R. Dolan, A. A. P. Trichet, B. D. Gerardot, J. M. Smith, *Appl. Phys. Lett.* **2018**, *112*, 191105.
- [21] N. Lundt, S. Klemmt, E. Cherotchenko, S. Betzold, O. Iff, A. V. Nalotov, M. Klaas, C. P. Dietrich, A. V. Kavokin, S. Höfling, C. Schneider, *Nat. Commun.* **2016**, *7*, 13328.
- [22] P. K. Jha, H. Akbari, Y. Kim, H. A. Atwater, *arXiv:2007.07811*, **2020**.
- [23] J.-H. Kim, S. Aghaeimeibodi, J. Carolan, D. E. Englund, E. Waks, *Optica* **2020**, *7*, 291.
- [24] S. Kim, J. E. Fröch, J. Christian, M. Straw, J. Bishop, D. Totonjian, K. Watanabe, T. Taniguchi, M. Toth, I. Aharonovich, *Nat. Commun.* **2018**, *9*, 2623.
- [25] P. K. Shandilya, J. E. Fröch, M. Mitchell, D. P. Lake, S. Kim, M. Toth, B. Behera, C. Healey, I. Aharonovich, P. E. Barclay, *Nano Lett.* **2019**, *19*, 1343.
- [26] N. V. P. Proscia, H. Jayakumar, X. Ge, G. Lopez-Morales, Z. Shotan, W. Zhou, C. A. Meriles, V. M. Menon, *Nanophotonics* **2020**, *9*, 2937.
- [27] T. Vogl, R. Lecamwasam, B. C. Buchler, Y. Lu, P. K. Lam, *ACS Photonics* **2019**, *6*, 1955.
- [28] N. R. Jungwirth, G. D. Fuchs, *Phys. Rev. Lett.* **2017**, *119*, 057401.
- [29] A. Dietrich, M. Bürk, E. S. Steiger, L. Antoniuk, T. T. Tran, M. Nguyen, I. Aharonovich, F. Jelezko, A. Kubanek, *Phys. Rev. B* **2018**, *98*, 081414(R).
- [30] I. H. Abidi, N. Mendelson, T. T. Tran, A. Tyagi, M. Zhuang, L.-T. Weng, B. Özyilmaz, I. Aharonovich, M. Toth, Z. Luo, *Adv. Opt. Mater.* **2019**, *7*, 1900397.
- [31] J. Comtet, E. Glushkov, V. Navikas, J. Feng, V. Babenko, S. Hofmann, K. Watanabe, T. Taniguchi, A. Radenovic, *Nano Lett.* **2019**, *19*, 2516.
- [32] D. Hunger, T. Steinmetz, Y. Colombe, C. Deutsch, T. W. Hänsch, J. Reichel, *New J. Phys.* **2010**, *12*, 065038.
- [33] N. Mendelson, Z.-Q. Xu, T. T. Tran, M. Kianinia, J. Scott, C. Bradac, I. Aharonovich, M. Toth, *ACS Nano* **2019**, *13*, 3132.
- [34] H. L. Stern, R. Wang, Y. Fan, R. Mizuta, J. C. Stewart, L.-M. Needham, T. D. Roberts, R. Wai, N. S. Ginsberg, D. Klenerman, S. Hofmann, S. F. Lee, *ACS Nano* **2019**, *13*, 4538.
- [35] S. Häußler, J. Benedikter, K. Bray, B. Regan, A. Dietrich, J. Twamley, I. Aharonovich, D. Hunger, A. Kubanek, *Phys. Rev. B* **2019**, *99*, 165310.
- [36] T. Grange, G. Hornecker, D. Hunger, J.-P. Poizat, J.-M. Gérard, P. Senellart, A. Auffèves, *Phys. Rev. Lett.* **2015**, *114*, 193601.
- [37] A. Dietrich, M. W. Doherty, I. Aharonovich, A. Kubanek, *Phys. Rev. B* **2020**, *101*, 081401(R).
- [38] M. Hoese, P. Reddy, A. Dietrich, M. K. Koch, K. G. Fehler, M. W. Doherty, A. Kubanek, *Sci. Adv.* **2020**, *6*, 40.
- [39] B. Casabone, J. Benedikter, T. Hümmer, F. Oehl, K. de Oliveira Lima, T. W. Hänsch, A. Ferrier, P. Goldner, H. de Riedmatten, D. Hunger, *New J. Phys.* **2018**, *20*, 095006.
- [40] J. M. Binder, A. Stark, N. Tomek, J. Scheuer, F. Frank, K. D. Jahnke, C. Müller, S. Schmitt, M. H. Metsch, T. Uden, T. Gehring, A. Huck, U. L. Andersen, L. J. Rogers, F. Jelezko, *Software X* **2017**, *6*, 85.